

Negative Capacitance for Stabilizing Logic State in Tunnel Field-Effect Transistor

Koushik Dey,^{1,†} Bikash Das,¹ Pabitra Kumar Hazra,¹ Tanima
Kundu,¹ Sanjib Naskar,² Soumik Das,¹ Sujan Maity,¹ Poulomi Maji,¹
Bipul Karmakar,¹ Rahul Paramanik,¹ and Subhadeep Datta^{1,‡}

¹*School of Physical Sciences, Indian Association for the Cultivation of Science,
2A & B Raja S. C. Mullick Road, Jadavpur, Kolkata - 700032, India*

²*Central Scientific Services, Indian Association for the Cultivation of Science,
2A & B Raja S. C. Mullick Road, Jadavpur, Kolkata 700032, India*

Abstract

Ferroelectric negative capacitance transistors, or Fe-NCFETs, are promising device architecture for achieving improved performance in terms of hysteresis, on-off ratio and power consumption. The study investigates the influence of negative capacitance (NC) on the transfer characteristics of van der Waals Field-Effect Transistors (vdW FETs) below and above a critical voltage (V_{th}) on the hetero phase of CuInP_2S_6 (CIPS) gate ferroelectric. Notably, a less pronounced NC resulting from the spatial distribution of the ferroelectric (FE) and paraelectric (PE) phases plays a crucial role in stabilizing of n-channel conductance by dual gate modulation. This results into the emergence of a non-volatile logic state, between the two binary states typical of conventional Tunnel Field-Effect Transistors (TFETs). Concerned study proposed negative capacitance tunnel field-effect transistors (NC-TFETs) based on ferroionic crystals as promising devices for generating a stable logic state below the coercive voltage. In addition, tunneling and voltage pinning effects play key role for enhancement of transistor's on-off ratio.

keywords: Negative capacitance, Field effect transistor, 2D ferroelectric, TMDs, Tunnel FET, logic state.

I. INTRODUCTION

Tunnel field-effect transistors (TFETs) have garnered a lot of attention due to their ability to achieve a steep subthreshold swing (SS) with band-to-band tunneling (BTBT) of carriers [1, 2]. However, the on-current of conventional TFETs is too low to be a viable substitute for metal oxide semiconductor field-effect transistors (MOSFET). Integrating ferroelectric (FE) materials with TFETs has been proved to be a useful way to overcome this important technological issues [3]. Ferroelectric materials exhibit negative capacitance (NC) region which in general highly unstable region and cannot be realized through experiments [4]. However, this NC effect can be stabilized by placing suitable dielectric in series with a FE capacitor [5, 6]. Furthermore, a MOS transistor's gate capacitance can be increased by integrating a ferroelectric capacitor into the gate stack, particularly when the transistor is functioning in the NC region [7]. This series architecture can act as a step up voltage

[†] koushikdey664@gmail.com

[‡] sspsdd@iacs.res.in

transformer, resulting in a sudden rise in the internal voltage which is proportional to the polarization of ferroelectric materials. Consequently, the probability of BTBT increases and the drain current enhances [8].

Nowadays, p-type metal oxide (MO) materials like SnO, CuO, and Cu₂O have attracted considerable attention due to their distinctive properties and potential applications in tunnel field-effect transistors (TFETs). Moreover, to facilitate monolithic three-dimensional (M3D) integration of high-performance logic, there is a strong demand for high-mobility p-type oxide semiconductor thin films. These thin films can be utilized in the fabrication of back-end-of-line (BEOL) compatible complementary metal-oxide-semiconductor (CMOS) circuits [9]. Among these, atomic layer deposited Cu-based oxide CMOS devices are promising for high performance in terms of high mobility, low off current etc [10–13]. Thus, these are attracting for real-world applications i.e, photonic, spectroscopic, photoelectronics and energy harvesting purposes [14–17].

On the contrary, wide-bandgap metal-oxide n-type semiconductors capable of sustaining a robust p-type inversion layer when paired with a high-dielectric-constant (HZO) barrier and sourced with a heterogeneous p-type material. The utility of this inversion layer as for controlling element in a unique tunnelling junction transistor result into remarkable characteristics, such as high current, power, and transconductance densities [18]. Here, we integrate a wide bandgap n-type transition metal dichalcogenides (TMDs) WS₂ paired with a ferroelectric material for TFET device architecture.

Transistors incorporating newly developed two-dimensional (2D) van der Waals (vdW) ferroelectric materials outperform conventional complementary metal-oxide-semiconductor FETs (CMOSFETs), exhibiting reduced power consumption, increased switching speed, and enhanced stability [19, 20]. The potential of vdWs FeFETs to surpass the limits of Moore’s law opens up new possibilities for exploration and utilization in nanoelectronics, particularly in nonvolatile memory and neuromorphic computing applications [21, 22]. The atomically thin channels of 2D semiconductors, like transition metal dichalcogenides (TMDs), provide ideal electrostatic control to improve immunity to short channel effects [23]. For this reason, they have been thoroughly investigated as channel materials for future electronic device applications. Negative capacitance field effect transistors (NCFETs) have been documented extensively using 2D TMDs as the channel material and ferroelectric materials such as hafnium zirconium oxide (HZO) as the ferroelectric gate [24]. In comparison to bulk

ferroelectrics, layered ferroelectrics with atomically smooth surfaces may provide superior performance and reliability for NC-FETs by minimizing the impact of dangling bonds and charged impurities that induce interface traps [25].

CuInP₂S₆ (CIPS) is such a ferroelectric 2D materials which exhibits switchable polarization down to 4 nm at room temperature [26] and enables interface integration for constructing vdW heterostructure-based functional memory and logic devices like NC-FETs, ferroelectric tunnel junctions (FTJs) etc [19, 27]. Moreover, CIPS is recognized for its significant electric-field controllable macroscopic ionic conductivity [28]. The interplay between this conductivity and ferroelectricity give rises to ferroionic states that can be useful for getting novel device performance [29]. It's worth mentioning that in cases of copper deficiency in CIPS, the system experiences a chemical phase separation, leading to the formation of a paraelectric (PE) In_{4/3}P₂S₆ (IPS) phase alongside ferroelectric CIPS phase [30]. The formation of FE-PE hetero-structure by spatial random distributions may results into performance variations when integrated on a TMD channel and may open up new possibilities for getting different logical devices [31].

To generate desirable and stable logical device, we have implemented two strategies i.e. NC modulation and the effect of long-range Cu ion migration in a vertical CIPS-IPS/WS₂ heterostructure. Here, we report the influence of NC on the transfer characteristics of vdW FETs below and above a critical voltage (V_{th}) on the CIPS-IPS gate. This study reveals the important role of a less pronounced NC resulting from the spatial distribution of the FE and PE phases for the stabilization of transconductance below the V_{th} , leading to the establishment of a nonvolatile logic state between the two binary states typical of conventional TFETs.

II. EXPERIMENTAL DETAILS

Synthesis and Characterization: CIPS single crystals were synthesized *via* standard chemical vapour transport (CVT) method by utilizing two zone tube furnace. Cu (99.95%, Alfa Aesar), In (99.95%, Alfa Aesar), P (99.95%, Alfa Aesar) and S (99.99%, Alfa Aesar) powders were mixed thoroughly in an atomic ratio 1:1:2:6. 5 mg/cc I₂ powder was used as transporting agent. The powders were thoroughly mixed and loaded into a quartz tube (25 cm) followed by evacuating the tube under 10⁻⁵ Torr vacuum, sealed and then placed in a

two-zone furnace. The temperature of the source zone was set to 750°C, and the growth zone to 650°C. After holding 7 days (168 hrs) at this temperature, the furnace was allowed to cool slowly to room temperature. CIPS single crystals were extracted by cleaving the chunk obtained inside the quartz tube. WS₂ single crystals were grown from starting material WS₂ micro-powder (99.95 % Sigma-Aldrich) by sealing the powders with I₂ in a quartz tube, followed by evacuation. The tube was kept in a horizontal two-zone tube furnace for seven days. The growth zone's temperature was set at 840°C, while the source zone's temperature was set to 920°C. The as-grown WS₂ single crystals were extracted from the tube's cold regime.

X-ray diffraction (XRD) measurements were carried out using Bruker diffractometer using Cu K_α source on single crystal and on fine powders. Scanning electron microscope (SEM) and energy-dispersive spectroscopic (EDS) study were also performed in a JEOL JSM-6010LA. Polarization electric field (PE) hysteresis loops were recorded at room temperature on a thin crystal by utilizing Radiant precision ferroelectric tester. The Raman measurements were performed with a 532 nm laser in the backscattering geometry using a Horiba T64000 single spectrometer with high-resolution grating and a CCD detector. Temperature dependent dielectric measurements were carried out on a wet cryostat (OXFORD Optistat CF) utilizing Zurich Instruments MFIA impedance analyzer and CRYOCON (22c) temperature controller. Capacitance under dc biases on flakes were recorded with the same impedance analyzer at room temperature. Two probe I-V measurements were carried out on thin flakes by utilizing 2601B source measure units (SMU). A commercial atomic force microscope (Asylum Research MFP-3D) equipped with Ti/Ir-coated Si cantilever tip was used to detect piezoresponse on thin crystal flakes transferred onto Indium Tin oxide (ITO) coated glass substrate by utilizing dual ac resonance tracking piezoresponse force microscopy (DART-PFM) mode. Several distinct random spots were chosen to measure the local piezoresponse hysteresis loops by varying tip bias voltage on flakes.

Device Fabrication and electrical characterization: After micromechanical exfoliation of WS₂ crystals using standard scotch tape, WS₂ flakes were transferred onto a clean SiO₂ (285 nm)/Si substrate. Suitable flakes were located by utilizing optical microscope (OLYMPUS BX53M) by comparing the flake's transparency. Thin flakes of CIPS-IPS crystal was exfoliated on PDMS gelpak and were integrated on top of each selected WS₂ flakes by utilizing a micromanipulator. After that, optical lithography was employed to create the

devices. Using a thermal evaporator, metal contacts were created with 10 nm Cr followed by 90 nm Au. Next, FET measurements were performed by utilizing SIGLENT’s SDG7000A arbitrary waveform generator, Keithley 2450 and 2601B (SMU).

III. RESULTS AND DISCUSSION

The as-grown single crystal exhibits transparent homogeneous colored thin sheets (see the inset of Figure 1a). The quality of the crystal is examined through X-ray diffraction (XRD) of *ab*-plane orientation. All diffraction peaks can be successfully indexed to (00*l*) peaks. SEM energy-dispersive X-ray spectroscopy (EDS) examination was carried out to verify the atomic stoichiometry of this sample. The compositions derived from the EDS analyses, presented in Table S1 are averages from typically around four data collection regions (see Figure S1 in the Supporting Information). The average stoichiometry is found to be Cu deficient with composition $\text{Cu}_{0.46}\text{In}_{1.21}\text{P}_{2.39}\text{S}_{5.93}$. Further, the structure refinement of the X-ray diffraction (XRD) pattern for these ground crystals has confirmed the presence of two different phases with $\sim 63\%$ CIPS and $\sim 37\%$ IPS. The detailed structural information along with the Rietveld refined XRD pattern is presented in the Supporting Information (see Figure S2 and Table S2).

The atomic structure of CIPS is characterized by Cu, In, and P–P triangular patterns occupying the octahedral spaces within the sulfur framework as shown in the Figure 1b. Weak van der Waals (vdW) interactions facilitate the vertical stacking of layers to form bulk crystals. A complete unit cell comprises two adjacent monolayers, essential for properly characterizing the material’s symmetry due to the exchange of Cu and P-P pairs between layers. Each layer of the monoclinic (space group *Cc*) CIPS crystal is made up of S_6 octahedra that encircle P-P pairs or metal cations (Cu, In) [32]. Together, the phosphorus atoms and the S_6 octahedra form a structural backbone consisting of $[\text{P}_2\text{S}_6]^{4-}$ anion groups that ionically link with Cu and In cations organized hexagonally (see Figure 1b). CIPS is a collinear two-sublattice ferrielectric system which exhibits a Curie temperature (T_C) of approximately 315 K [33]. In the ferrielectric phase below T_C , spontaneous polarization occurs with the polar axis perpendicular to the layer plane. This polarization results from off-center ordering in the Cu sublattice and the displacement of cations from centrosymmetric sites in the In sublattice [34]. Notably, when Cu deficits are present in CIPS, the material

spontaneously phases out into paraelectric $\text{In}_{4/3}\text{P}_2\text{S}_6$ (IPS) with centrosymmetric crystal structure (space group $P2_1C$) [30] and ferroelectric CIPS domains inside the same single crystal, sharing an anionic $[\text{P}_2\text{S}_6]^{4-}$ (see Figure 1c).

To further confirm the presence of two different composition and to check the homogeneity of these two phases, we have collected Raman spectra on several regions of a bulk crystal and on exfoliated flakes with different thicknesses. The room temperature representative Raman spectrum of bulk crystal and flake are depicted in Figure 1d. There are 27 number of modes which can be resolved in those Raman spectra, attributed to the presence of both CIPS and IPS sub-lattices within the material by comparing with the reported Raman spectra of pure CIPS and CIPS-IPS heterophase [36, 37]. The increased number of modes in our Raman spectra is consistent with the CIPS-IPS Raman spectra of earlier reports. Interestingly, the Raman spectrum of the flake agrees well with that of bulk crystal which assures chemically homogeneous distribution of CIPS and IPS phases down to few layer flakes.

Above 100 cm^{-1} , four different modes are observed in the anion translation region, ranging from 100 to 140 cm^{-1} . Among these modes, two (at $\sim 100\text{ cm}^{-1}$ and $\sim 114\text{ cm}^{-1}$) are attributed to CIPS, while the other two (127 cm^{-1} and 140 cm^{-1}) are assigned to IPS [35]. Similarly, in the range of 200 to 300 cm^{-1} , the two most intense peaks are observed at ~ 255 and $\sim 270\text{ cm}^{-1}$, corresponding to IPS and CIPS, respectively. Generally, mode at $\sim 300\text{ cm}^{-1}$ can not be seen in the pure CIPS, which is attributed to anion deformation in IPS [37]. Whereas, the mode at $\sim 320\text{ cm}^{-1}$ is assigned to anion deformation in CIPS. Raman modes at ~ 580 and $\sim 610\text{ cm}^{-1}$ do not appear in the CIPS Raman spectrum and are considered as the anion stretching modes of IPS [35].

The interplay between the two sub-lattices in the CIPS-IPS heterostructure causes the IPS domains to exert a chemical pressure over the CIPS domains, increasing the overall T_C to approximately $320\text{-}335\text{ K}$ for substantially Cu-deficient CIPS [38]. Temperature-dependent dielectric results at selected frequencies are presented in Figure 1(e-f). At low frequencies, dielectric losses rise with increasing temperature, resulting in an increase in the real part of the dielectric permittivity. This effect is primarily due to high conductivity [39]. At higher frequencies, the real part of the dielectric permittivity aligns with the static permittivity, due to the significant decrement of $\tan\delta$. It has been observed that Cu deficiencies or the addition of extra In ions significantly alter the ferroelectric phase transition temperature. From temperature-dependent dielectric measurements, a phase transition can be readily

seen at around 328 K (maximum temperature of static dielectric permittivity), indicating a paraelectric to ferroelectric phase transition occurring at a higher temperature compared to pure CIPS. In order to confirm the ferroelectric properties of this material, polarization (P) vs out-of-plane electric field (E) data was measured on a thick flake. The presence of a distinct hysteresis loop (see the inset of Figure 1f) is a direct evidence of ferroelectricity with coercive field (E_c) ~ 16.4 kV/mm and remanent polarization (P_r) ~ 3.42 $\mu\text{C}/\text{cm}^2$. We have recorded temperature dependent P-E loops on CIPS-IPS bulk crystals below and above the ferroelectric to paraelectric phase transition temperature, presented in the Supporting Information. Polarization loops and the corresponding current density loops at selected temperatures are shown in Figure S3(a-c). The polarization loops getting wider as we increased temperature. The changes in loop shape (*i.e.*, loop edges shift towards electric field axis with larger loop area) at higher fields and higher temperatures are due to the generation of larger leakage currents. From the current density plots, an abrupt increment of currents at higher fields (in FE phase) and almost linear rise of currents with fields (in PE phase) can be clearly seen. This indicates a strong coupling of ferroelectric polarization with ionic conduction in the CIPS-IPS heterophase. From temperature dependent E_c (see the inset in Figure S3) it can be seen that CIPS-IPS completely loses its ferroelectric nature above 328 K.

Next, we focus on piezoresponse force microscopy (PFM) results of CIPS-IPS flakes exfoliated on a metal substrate to investigate thin flake ferroelectric and piezoelectric properties. Figure 2a illustrates the smooth topography of a representative CIPS-IPS flake. Fig. 2b and 2c represents PFM amplitude and phase map of the mentioned region. Indeed, the PFM amplitude serves as an indicator of the absolute magnitude of the local piezoelectric response. Simultaneously, the PFM phase provides information about the polarization direction within each individual domain. These measurements are valuable for characterizing the piezoelectric and ferroelectric properties of materials at the nanoscale [40].

PFM measurements can distinguish between regions of different piezoresponse in the sample by closely examining the local piezoresponse of different regions within the flake. As illustrated in Figure 1e-f the CIPS ferroelectric phase with upward and downward direction polarization domains are identified with higher & lower PFM amplitude between those regions (arrows indicate polarization direction of the shaded regions). A clear 180°C phase difference is observed between the upward- and downward-polarized ferroelectric domains

within the CIPS phase. However, the IPS paraelectric phase shows negligible piezoresponse. This observation indicates CIPS and IPS regions spatially extends upto several nanometers. To further check piezoresponse in those mentioned regions we have recorded local PFM amplitude and phase hysteresis loops by varying dc bias, as shown in Figure 2e-f. CIPS region exhibits a well defined strain and phase loop with a remanence, confirming ferroelectric nature of CIPS. Whereas, the IPS region shows a negligible strain and phase hysteresis loops similar like paraelectric phase.

To investigate the electric properties of CIPS-IPS flake, a vertical sandwiched Au/CIPS-IPS/Au device is fabricated [see inset of Figure 3a]. I-V loops are measured at room temperature depicted in Fig. 3 (a). The cycled I-V curve reveals significant current hysteresis with a clockwise direction (shown by arrow). The magnitude of the hysteresis window strongly depends on the range of the maximum voltages. Notably, when examining the voltage sweep within the range of ± 4 volts (red), negligible current is observed. However, as the voltage range exceeds ± 5 V, the current starts to increase rapidly. The hump at around ± 3 volt (shown by dashed arrows) indicates current increment for polarization switching (nearby V_c), which typically drops above that for typical ferroelectrics. However, at higher voltages, a steep rise in current indicates the onset of long-range conduction. A sudden increment of dielectric loss ($\tan\delta$) is also seen around the same voltage (see in Figure 3b) which corroborates long range conduction at higher voltages.

The presence of ferroelectricity and paraelectricity in thin flakes can be obtained from the quasistatic capacitance-voltage (C-V) measurements [41]. C-V measurement involves superimposing a small amplitude AC voltage (to measure C) over a DC voltage (P). We have applied 500 mV peak-to-peak ac signal with 300 kHz frequency superimposed with a dc bias (varying upto ± 6 V) for the measurements. The two peaks in C-V characteristics (shown in Figure 3b) associated with the ferroelectric switching phenomena. An imprint voltage of around 2 V is observed in the hysteresis loop of the C-V curve, indicating the presence of an internal electric field between electrodes. The internal electric field may generate due to the gradient in the strain distribution in the flake or a non-homogeneous spatial distribution of defects like Cu^+ vacancies [42].

All the presented evidence unambiguously confirms the existence of FE-PE heterophases in the 2D CIPS-IPS, positioning it as a promising non-volatile element in vdW heterostructures. The material is then tested for its applications in a prototype FEFET. The vdW

heterojunction is fabricated by exfoliating thin CIPS-IPS flakes onto WS₂ channel material on a Si/SiO₂ substrate, can be seen in the optical micrograph of Figure 4a. The experimental configuration of FeFET is depicted in Figure 4b, where a ferroelectric capacitor is integrated externally with the top gate of WS₂/SiO₂. This approach enables the identification of the best match between the negative capacitance (NC) of the ferroelectric and the intrinsic capacitance of the transistor's gate. The equivalent capacitance network can be seen in Figure 4c. The NCFET integrates a ferroelectric material into the gate stack of the transistor, demonstrating negative capacitance under specific conditions. Within the NCFET's metal-ferroelectric-insulator-semiconductor (MFIS) configuration, the arrangement can be analogously depicted as a capacitor divider circuit comprising the ferroelectric capacitance, C_{FE} , and the inherent baseline FET capacitance, C_{int} , as illustrated in Figure 4c. An inverse C_{FE} yields voltage amplification (A_V) at the internal gate, where $A_V = \frac{|C_{FE}|}{|C_{FE}| - C_{int}}$ [4]. The internal voltage amplification plays a crucial role in surpassing the sub-threshold swing beyond the Boltzmann limit. Furthermore, it leads to a higher ON current in NCFET compared to the baseline FET under the same applied voltage. From a thermodynamic perspective, any equilibrium ferroelectric system can be characterized by a double well energy profile at zero applied electric field, as depicted in Figure 4d. This energy profile features three extremal states: two with positive curvature or positive capacitance minima, and one with negative curvature or a NC maximum, where capacitance equals $(\frac{\partial^2 G}{\partial P^2} - 1)$ and the energy profile can be understood from the Landau-Khalatnikov (L-K) theory [43]. The system typically occupies one of the two states of minimum energy corresponding to a nonzero or remnant polarization at zero bias. The NC state associated with the energy maximum is unstable and thus inaccessible in an isolated ferroelectric capacitor. Salahuddin and Datta [4] proposed to stabilize the typically unstable NC state by introducing a positive dielectric capacitance in series with the ferroelectric, thereby ensuring a positive total capacitance for the system. By employing this technique, a stable minimum in the total energy of the system (at P_0) is achieved, with the ferroelectric residing in the NC state, as depicted in Figure 4d. In the structure of an NCFET, the internal baseline FET serves as a positive capacitance (C_{int}) (Figure 4d), capable of stabilizing the ferroelectric in the NC state if the total gate capacitance $(\frac{1}{C_{int}} + \frac{1}{C_{FE}})^{-1}$ is positive. This condition necessitates that $|C_{FE}|$ must exceed C_{int} to realize a thermodynamically stable NC state of the ferroelectric in the NCFET.

Figure 4e illustrates the input transfer characteristic of an n-type Negative Capacitance

NC-FET. The bottom gate voltage (V_{bg}) is swept from -10 V to +30 V and back to the starting point while the drain voltage (V_{sd}) is set to 3 V. Different curves are plotted with varying top gate voltages (V_{tg}) to visualize the impact of it on the transfer characteristics (I_{sd} - V_{bg}). At zero top gate voltage, a relatively large clockwise hysteresis loop is obtained, typically attributed to the presence of interface traps [44]. Substantial reduction in hysteresis loop in I_{sd} - V_{bg} occurs after the application of a small negative bias at top gate, indicating that the gentle decline characteristic corresponds to the NC effect. Surprisingly, a steeper off-to-on transition of the drain current I_{sd} is observed when the negative top gate voltages are set at and above 5 Volts. Exactly similar but opposite behavior is obtained on the transfer characteristics for positive V_{tg} as shown in Figure 4f. The ON/OFF ratio obtained from the transfer characteristics is plotted against V_{tg} and found three different regions, shown in Figure 4g. At higher positive and negative V_{tg} , after getting sufficient energies the Cu ions starts to migrate through the vdW layers by finding channels through Cu vacancies which remained inactive so far. For higher positive V_{tg} , the Cu ions starts to get accumulated near the positively polarized bound charges and the n-channel. Consequently, n-channel carriers get depleted into CIPS-IPS layers via air gap and interfacial gap between WS_2 and CIPS-IPS instead of going towards source to drain. For sufficiently large negative bias V_{tg} , Cu ions migrate along gate terminal and get accumulated there and carriers from CIPS-IPS regions get depleted into n-channel. Otherwise, at sufficiently lower V_{tg} , when Cu ions cannot participate in long-range conduction, leakage through the FE is negligible and NC effect dominates. At that voltages ($\leq V_{th}$), the ON-OFF ratio follows usual trends (see the zoomed view of ON-OFF ratio in Figure 4g). The channel transconductance (dI_{sd}/dV_{bg}) against V_{tg} are plotted for different V_{bg} are shown in Figure 4h. A stable transconductance is obtained for $\leq V_{th}$ which signifies a different state in between two binary state of TFETs. The intermediate logic state in between conventional ON and OFF can be useful to create logic devices with additional logic ‘1/2’ state in between ‘0’ and ‘1’ states. This logic ‘1/2’ state can be obtained by dual gate modulation. We have also measured channel currents as a function of ferroelectric gate voltage (at zero V_{bg}). When the applied voltage (V) exceeds a critical voltage, macroscopic polarization develops into CIPS-IPS, and the device enters the “On” state (see Figure 4i). In this voltage range, intralayer and interlayer Cu ion hopping begins, leading to significant ionic conduction in CIPS-IPS. Consequently, once this critical field is reached, tunneling from the channel to the gate occurs, and the device characteristics

enter the region of negative differential resistance (NDR). The tunnelling current direction will get reversed for sufficiently high negative gate bias. This tunnelling phenomena is shown pictorially by 2D schematics (Figure 4j).

IV. CONCLUSION

In conclusion, negative capacitance Tunnel Field-Effect Transistors (TFETs) based on ferroionic crystals are proposed as one of the most promising devices to generate a stable non-volatile logic state. Experimental validation demonstrates that a less prominent Negative Capacitance (NC) based on a ferroelectric-paraelectric (FE-PE) heterostructure provides beneficial effects on TFET operation and digital performances. This includes an improved off-to-on transition and an extended stable region below the coercive voltage of the NC ferroelectric, facilitated by the tunneling and voltage pinning effects of the ferroelectric material. The study suggests the potential of these devices for stable and efficient non-volatile logic applications.

Supporting Information Detailed scanning electron microscopy, X-ray diffraction and temperature dependent ferroelectric characterizations supplied as Supporting Information.

ACKNOWLEDGMENTS

KD would like to acknowledge CSS facilities (XRD, SEM, AFM) of IACS. SD also acknowledges support (lithography facility) from the Technical Research Centre (TRC), IACS, Kolkata. The financial supports from IACS, DST-INSPIRE and CSIR-UGC are greatly acknowledged. SD acknowledges the financial support from DST-SERB grant No. CRG/2021/004334 and special grant SCP/2022/000411.

S.D., and K.D. conceived the project and designed the experiments. K.D., and B.D. prepared the samples and performed their initial characterization together. K.D., and B.D. performed PFM measurements with the help of S.N. and analyzed the data. Raman measurements and analysis were carried out by K.D. and S. Das. Device fabrication and modification were carried out by T.K., K.D. along with P.K.H., B.K., S.M., P.M., R.P. K.D., B.D., T.K. and R.P. performed the electrical measurements on device and analyzed the data. All

authors discussed the results and actively commented on the manuscript written by K.D. and S.D.

-
- [1] Kao, K. H., Verhulst, A. S., Vandenberghe, W. G., Soree, B., Groeseneken, G., De Meyer, K. Direct and indirect band-to-band tunneling in germanium-based TFETs. *IEEE Transactions on Electron Devices*, **2011**, 59(2), 292-301.
 - [2] Lee, M. H., Wei, Y. T., Lin, J. C., Chen, C. W., Tu, W. H., Tang, M. J. A. A. Ferroelectric gate tunnel field-effect transistors with low-power steep turn-on. *AIP Advances*, **2014**, 4(10).
 - [3] Dewey, G., Chu-Kung, B., Boardman, J., Fastenau, J. M., Kavalieros, J., Kotlyar, R., Liu, W.K., Lubyshev, D., Metz, M., Mukherjee, N. and Oakey, P., (2011, December). Fabrication, characterization, and physics of III–V heterojunction tunneling field effect transistors (H-TFET) for steep sub-threshold swing. *In 2011 International electron devices meeting* (pp. 33-6). IEEE.
 - [4] Salahuddin, S., Datta, S. Use of negative capacitance to provide voltage amplification for low power nanoscale devices. *Nano letters*, **2008**, 8(2), 405-410.
 - [5] Saeidi, A., Farzan J., Igor S., and Adrian M. I. Double-gate negative-capacitance MOSFET with PZT gate-stack on ultra thin body SOI: An experimentally calibrated simulation study of device performance. *IEEE Transactions on Electron Devices*, **2016**, 63(12), 4678-4684.
 - [6] Khan, A. I., Chatterjee, K., Wang, B., Drapcho, S., You, L., Serrao, C., Bakaul, S.R., Ramesh, R. and Salahuddin, S. Negative capacitance in a ferroelectric capacitor. *Nature materials*, **2015**, 14(2), 182-186.
 - [7] Park, J. H., Jang, G. S., Kim, H. Y., Seok, K. H., Chae, H. J., Lee, S. K., Joo, S. K. Sub-kT/q subthreshold-slope using negative capacitance in low-temperature polycrystalline-silicon thin-film transistor. *Scientific reports*, **2016**, 6(1), 24734.
 - [8] Kobayashi, M. Hiramoto, T. On device design for steep-slope negative-capacitance field-effect-transistor operating at sub-0.2 V supply voltage with ferroelectric HfO₂ thin film. *AIP Advances*, **2016**, 6(2).
 - [9] Bae, H, Charnas A, Chung W, Si M, Lyu X, Sun X, Park J, Wang H, Zemlyanov D, Peide DY. Ultrathin transparent Copper (I) oxide films grown by plasma-enhanced atomic layer deposition for Back-end-of-line p-Type transistors. *Nano Express*, **2021**, 2(2), 020023.

- [10] Maeng. W, Lee. SH, Kwon. JD, Park. J, Park. JS. Atomic layer deposited p-type copper oxide thin films and the associated thin film transistor properties. *Ceramics International*, **2016**, 425517.
- [11] Shen C, Yin Z, Collins F, Pinna N. Atomic layer deposition of metal oxides and chalcogenides for high performance transistors. *Advanced Science* **2022**, 9(23), 2104599.
- [12] Lee JH, Kim J, Jin M, Na HJ, Lee H, Im C, Kim YS. Cu₂O p-type thin-film transistors with enhanced switching characteristics for CMOS logic circuit by controlling deposition condition and annealing in the N₂ atmosphere. *ACS Applied Electronic Materials*, **2023**, 5(2), 1123-1130.
- [13] Shih CW, Chin A. New material transistor with record-high field-effect mobility among wide-band-gap semiconductors. *ACS Applied Materials & Interfaces.*, **2016**, 8(30), 19187.
- [14] Gyawali S, Tirumala RT, Loh H, Andiappan M, Bristow AD. Photocarrier Recombination Dynamics in Highly Scattering Cu₂O Nanocatalyst Clusters. *The Journal of Physical Chemistry C*. **2024**.
- [15] Huang CJ, Ya ZS, Horng JH, Hounng MP, Wang YH. GaAs metal-oxide-semiconductor field effect transistors fabricated with low-temperature liquid-phase-deposited SiO₂. *Japanese journal of applied physics*, **2002**, 41(9R), 5561.
- [16] Mohammadparast F, Ramakrishnan SB, Khatri N, Tirumala RT, Tan S, Kalkan AK, Andiappan M. Cuprous oxide cubic particles with strong and tunable Mie resonances for use as nanoantennas. *ACS Applied Nano Materials* **2020** 3(7), 6806.
- [17] Gyawali S, Tirumala RT, Andiappan M, Bristow AD. Size-and Shape-Dependent Charge-Carrier Dynamics in Sub-micron Cuprous Oxide Nanoparticles. *In Frontiers in Optics*, **2022**, Optica Publishing Group, JTU4A-86.
- [18] Shoute G, Afshar A, Muneshwar T, Cadien K, Barlage D. Sustained hole inversion layer in a wide-bandgap metal-oxide semiconductor with enhanced tunnel current. *Nature communications* **2016**, 7(1), 10632.
- [19] Wang, X., Yu, P., Lei, Z., Zhu, C., Cao, X., Liu, F., You L, Zeng Q, Deng Y, Zhu C, Zhou J. Van der Waals negative capacitance transistors. *Nature communications*, **2019**, 10(1), 3037.
- [20] Si, M., Liao, P. Y., Qiu, G., Duan, Y., Ye, P. D. Ferroelectric field-effect transistors based on MoS₂ and CuInP₂S₆ two-dimensional van der Waals heterostructure. *Acs Nano*, **2018**, 12(7), 6700-6705.

- [21] Venema, L. Silicon electronics and beyond. *Nature*, **2011**, 479(7373), 309-309.
- [22] Duhan, S., Tomer, V. Advanced Electronics: Looking beyond Silicon. *Advanced Energy Materials*, **2014**, 295-325.
- [23] Desai, S.B., Madhvapathy, S.R., Sachid, A.B., Llinas, J.P., Wang, Q., Ahn, G.H., Pitner, G., Kim, M.J., Bokor, J., Hu, C. and Wong, H.S.P. MoS₂ transistors with 1-nanometer gate lengths. *Science*, **2016**, 354(6308), 99-102.
- [24] Chen, L., Wang, L., Peng, Y., Feng, X., Sarkar, S., Li, Li, B., Liu, L., Han, K., Gong, X. and Chen, J., A van der Waals synaptic transistor based on ferroelectric Hf_{0.5}Zr_{0.5}O₂ and 2D tungsten disulfide. *Advanced Electronic Materials*, **2020**, 6(6), 2000057.
- [25] Zubko, P., Gariglio, S., Gabay, M., Ghosez, P., Triscone, J. M. (2011). Interface physics in complex oxide heterostructures. *Annu. Rev. Condens. Matter Phys.*, **2011**, 2(1), 141-165.
- [26] Io, W. F., Pang, S. Y., Wong, L. W., Zhao, Y., Ding, R., Mao, J., ... Hao, J. Direct observation of intrinsic room-temperature ferroelectricity in 2D layered CuCrP₂S₆. *Nature Communications*, **2023**, 14(1), 7304.
- [27] Jia, T., Chen, Y., Cai, Y., Dai, W., Zhang, C., Yu, L., Yue, W., Kimura, H., Yao, Y., Yu, S. and Guo, Q. Ferroelectricity and Piezoelectricity in 2D Van der Waals CuInP₂S₆ Ferroelectric Tunnel Junctions. *Nanomaterials*, **2022**, 12(15), 2516.
- [28] Jiang, X., Wang, X., Wang, X., Zhang, X., Niu, R., Deng, J., Xu, S., Lun, Y., Liu, Y., Xia, T. and Lu, J., Manipulation of current rectification in van der Waals ferroionic CuInP₂S₆. *Nature communications*, **2022**, 13(1), 574.
- [29] Zhang, D., Luo, Z. D., Yao, Y., Schoenherr, P., Sha, C., Pan, Y., ... Seidel, J. (2021). Anisotropic ion migration and electronic conduction in van der Waals ferroelectric CuInP₂S₆. *Nano letters*, **2021**, 21(2), 995-1002.
- [30] usner, M.A., Belianinov, A., Borisevich, A., He, Q., Chyasnavichyus, M., Demir, H., Sholl, D.S., Ganesh, P., Abernathy, D.L., McGuire, M.A. and Maksymovych, P. High-T c layered ferrielectric crystals by coherent spinodal decomposition. *ACS nano*, **2015**, 9(12), 12365-12373.
- [31] Kao, M.Y., Sachid, A.B., Lin, Y.K., Liao, Y.H., Agarwal, H., Kushwaha, P., Duarte, J.P., Chang, H.L., Salahuddin, S. and Hu, C. Variation caused by spatial distribution of dielectric and ferroelectric grains in a negative capacitance field-effect transistor. *IEEE Transactions on Electron Devices*, **2018**, 65(10), 4652-4658.

- [32] Maisonneuve, V., Evain, M., Payen, C., Cajipe, V. B., Molinie, P. Room-temperature crystal structure of the layered phase $\text{CuInIIP}_2\text{S}_6$. *Journal of alloys and compounds*, **1995**, 218(2), 157-164.
- [33] Simon, A., Ravez, J., Maisonneuve, V., Payen, C., Cajipe, V. B. Paraelectric-ferroelectric transition in the lamellar thiophosphate CuInP_2S_6 . *Chemistry of materials*, **1994**, 6(9), 1575-1580.
- [34] Maisonneuve, V., Cajipe, V. B., Simon, A., Von Der Muhll, R., Ravez, J. J. P. R. B. Ferrielectric ordering in lamellar CuInP_2S_6 . *Physical Review B*, **1997**, 56(17), 10860.
- [35] Rao, R., Selhorst, R., Conner, B. S., Susner, M. A. Ferrielectric-paraelectric phase transitions in layered CuInP_2S_6 and $\text{CuInP}_2\text{S}_6\text{-In}_{4/3}\text{P}_2\text{S}_6$ heterostructures: A Raman spectroscopy and x-ray diffraction study. *Physical Review Materials* **2022**, 6(4), 045001.
- [36] Sourisseau, C., Forgerit, J. P., Mathey, Y. Vibrational study of the $[\text{P}_2\text{S}_4^{-6}]$ anion, of some MPS_3 layered compounds ($\text{M} = \text{Fe}, \text{Co}, \text{Ni}, \text{In}$), and of their intercalates with $[\text{Co}(\eta^5\text{-C}_5\text{H}_5)_2]$ cations. *Journal of Solid State Chemistry*, **1983**, 49(2), 134-149.
- [37] Vysochanskii, Y. M., Stephanovich, V. A., Molnar, A. A., Cajipe, V. B., Bourdon, X. (1998). Raman spectroscopy study of the ferrielectric-paraelectric transition in layered CuInP_2S_6 . *Physical Review B*, **1998**, 58(14), 9119.
- [38] Checa, M., Jin, X., Millan-Solsona, R., Neumayer, S.M., Susner, M.A., McGuire, M.A., O'Hara, A., Gomila, G., Maksymovych, P., Pantelides, S.T. Collins, L. Revealing fast cation transport and enhanced conductivity at the $\text{CuInP}_2\text{S}_6\text{-In}_{4/3}\text{P}_2\text{S}_6$ heterointerface. *ACS nano*, **2022**, 16(9), 15347-15357.
- [39] Banys, J., Macutkevicius, J., Samulionis, V., Brilingas, A., Vysochanskii, Y. Dielectric and ultrasonic investigation of phase transition in CuInP_2S_6 crystals. *Phase Transitions*, **2004**, 77(4), 345-358.
- [40] Buragohain, P., Lu, H., Richter, C., Schenk, T., Kariuki, P., Glinsek, S., Funakubo, H., Íñiguez, J., Defay, E., Schroeder, U. Gruverman, A., Quantification of the Electromechanical Measurements by Piezoresponse Force Microscopy. *Advanced Materials*, **2022**, 34(47), 2206237.
- [41] Choi, W., Kim, S., Jin, Y. W., Lee, S. Y., Sands, T. D. Capacitance-voltage modeling of metal-ferroelectric-semiconductor capacitors based on epitaxial oxide heterostructures. *Applied Physics Letters*, **2011**, 98(10).

- [42] Boni, A. G., Chirila, C. F., Negrea, R., Ghica, C., Pasuk, I., Pintilie, I., Pintilie, L. Electrical Properties of Epitaxial Ferroelectric Heterostructures. *Epitaxy*, **2018**, 67.
- [43] Amrouch, H., Pahwa, G., Gaidhane, A. D., Henkel, J., Chauhan, Y. S. (2018). Negative capacitance transistor to address the fundamental limitations in technology scaling: Processor performance. *IEEE Access*, **2018**, 6, 52754-52765.
- [44] Kaushik, N., Mackenzie, D.M.A., Thakar, K. et al. Reversible hysteresis inversion in MoS₂ field effect transistors. *npj 2D Mater Appl*, **2017**, 1, 34.
- [45] Kobayashi, M., Jang, K., Ueyama, N., Hiramoto, T. Negative capacitance for boosting tunnel FET performance. *IEEE Transactions on Nanotechnology*, **2017**, 16(2) 253.
- [46] Zhao, M., Gou, G., Ding, X., Sun, J An ultrathin two-dimensional vertical ferroelectric tunneling junction based on CuInP₂S₆ monolayer. *Nanoscale*, **2020**, 12(23), 12522.

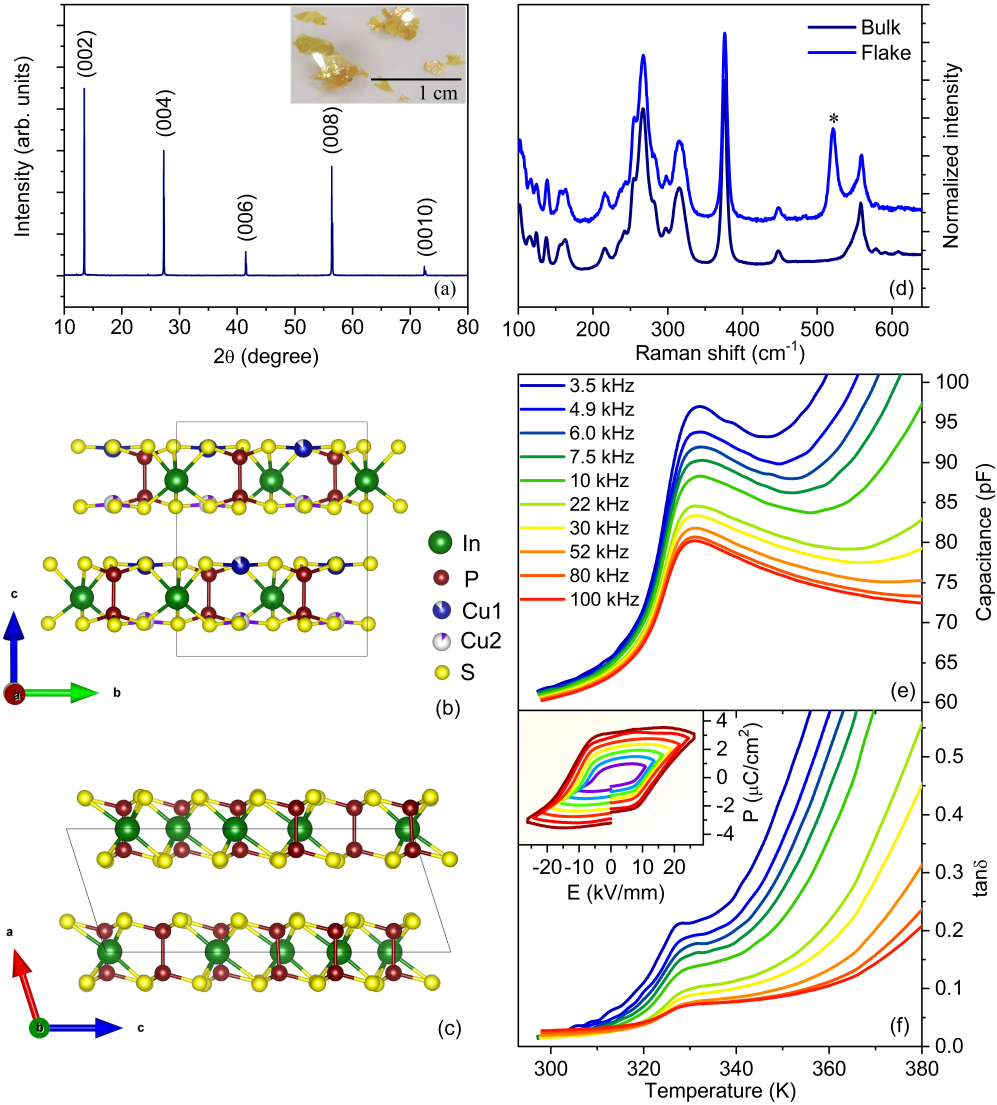


FIG. 1. (a) X-ray diffraction pattern of ab crystalline plane of the single crystal. Crystal structure of (b) CIPS & (c) IPS with vdW gap between the layers. The inset shows the as grown single crystals. (b) Room temperature Raman spectra of bulk crystal and thin flake. The starred mode corresponds to the characteristic mode of the Si wafer. Temperature dependence of (c) capacitance and (d) dielectric loss of the crystal at different frequencies. Frequency independent maxima ~ 328 K in (c) & (d) suggests a structural phase transition occurs at that temperature. The inset in (d) shows the trend of P-E loops up to various maximum electric fields at the same frequency.

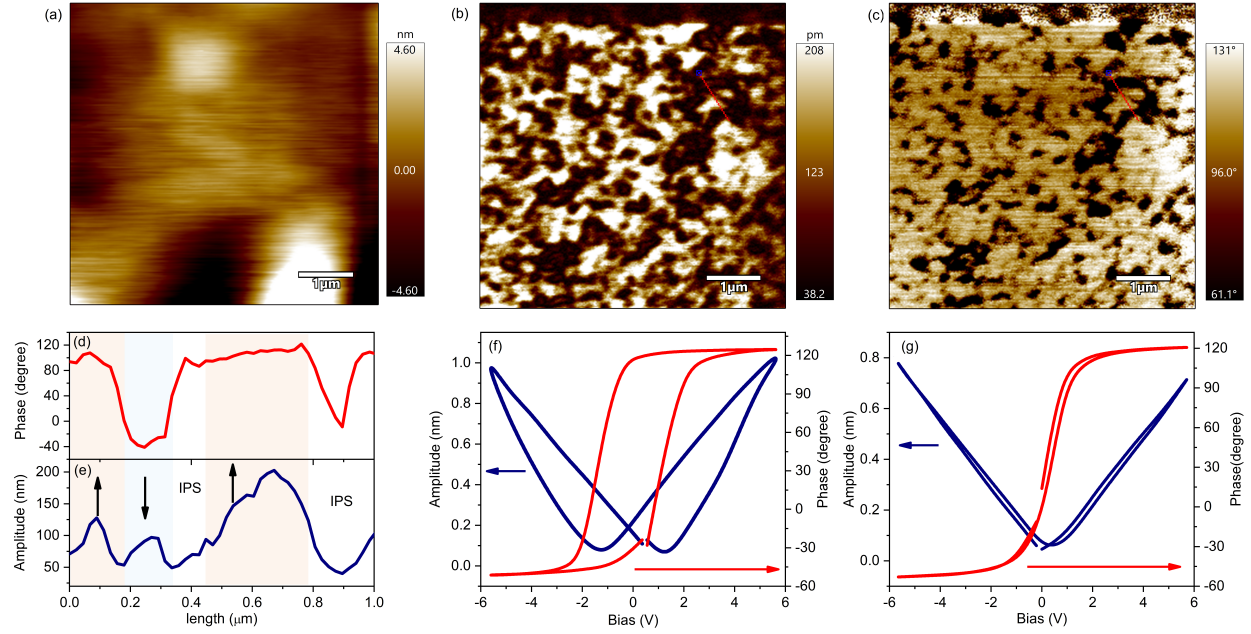


FIG. 2. (a) Topography, (b) PFM amplitude and (c) PFM phase images of the selected region of an exfoliated flake on ITO substrate. The line profile signals (red lines in (b) and (c)) of (d) PFM phase and (e) amplitude. A combination of these two signals separate out chemically different regions of CIPS-IPS self assembled hetero-structures. Arrow indicates polarization direction of domains of CIPS. Local PFM amplitude and phase hysteresis loops with dc bias on (f) CIPS and (g) IPS regions.

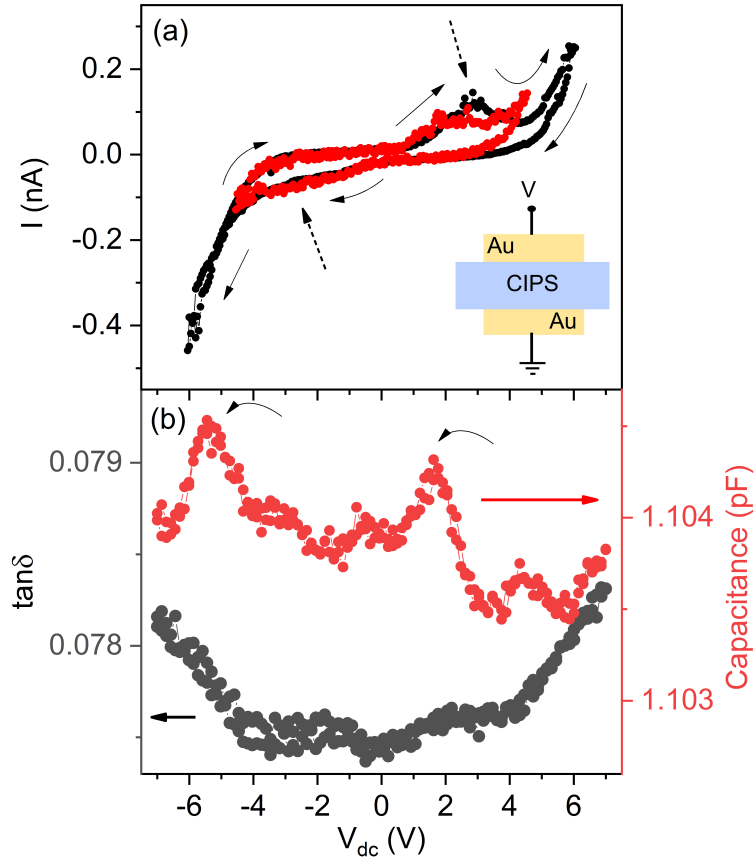


FIG. 3. (a) I-V curve of CIPS-IPS flake up to different maximum voltages on MIM device (schematic). Line arrows indicate the current path. Thick dashed arrow indicates two different humps where a broad current peaks appear due to polarization switching (b) Capacitance and dielectric loss *vs.* dc bias. Two capacitance peak marked as curved arrows indicate polarization switching at those voltages.

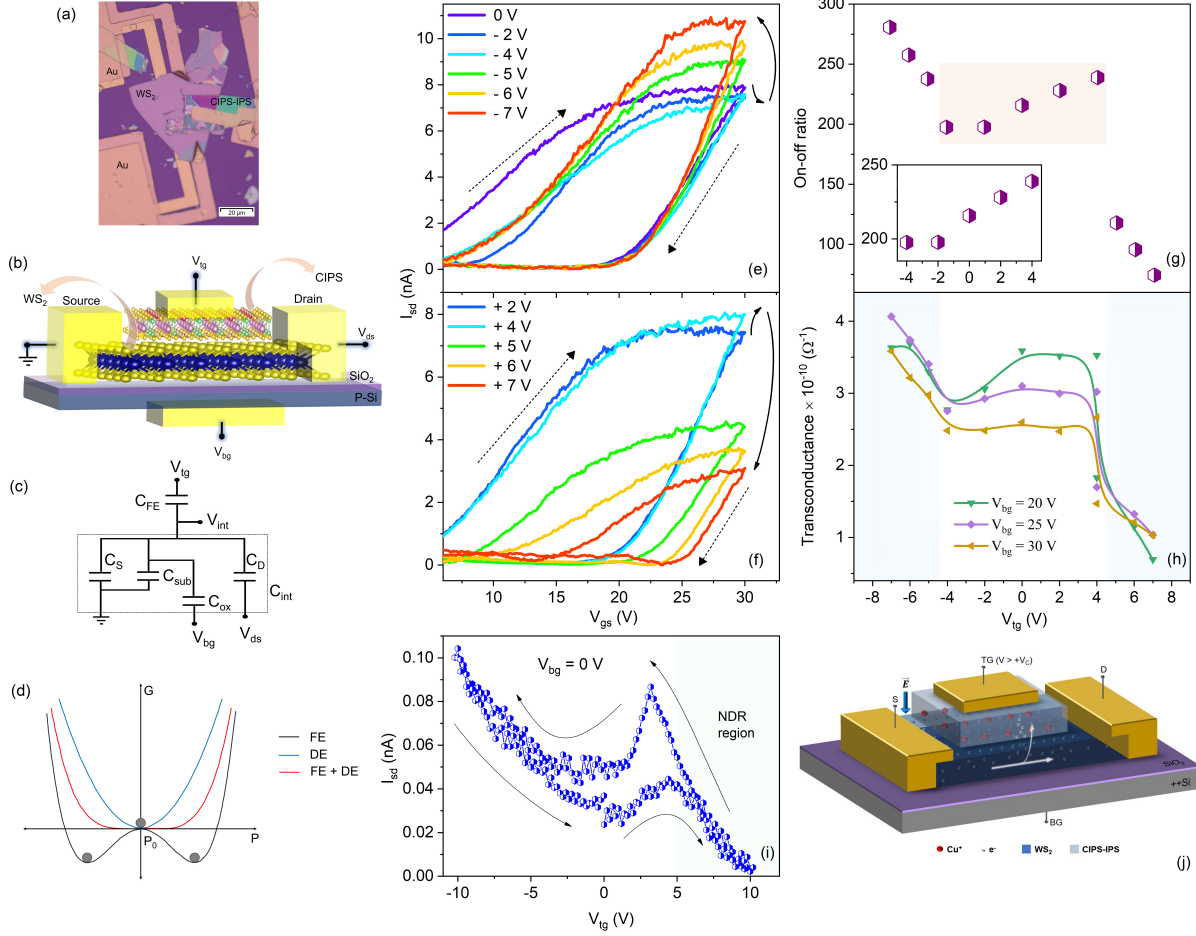


FIG. 4. (a) Optical micrograph of CIPS-IPS/ WS_2 heterostructure integrated on SiO_2/Si substrate. (b) Schematic diagram of dual gate experiments on that heterostructure. (c) Equivalent capacitance model of NC-FET. (d) Gibbs free energy profiles at zero external electric field, plotted as a function of polarization, for ferroelectric (FE), dielectric (DE), and the combined system (FE+DE). For typical ferroelectrics, one of the two energy minima is occupied. However, when a dielectric is added in series with the ferroelectric, the energy profile of the system changes. A minimum is observed at P_0 , where the ferroelectric resides in the negative capacitance state. I_{ds} - V_{bg} characteristics at different (e) negative and (f) positive top gate voltages. Dashed arrows show clockwise hysteresis loops of these characteristics. (g) ON-OFF current ratio and (h) transconductance as a function of top gate voltage. (i) Variation of I_{ds} with V_{tg} at zero back gate voltage. Line arrow shows a counterclockwise I_{ds} loop with top gate voltages. The shaded region shows negative differential resistance (NDR) state above a critical voltage. (j) Schematic representation of tunneling of charge carriers from channel to CIPS-IPS at some critical voltage.